



Article

Geohazard Plugin: A QGIS Plugin for the Preliminary Analysis of Landslides at Medium–Small Scale

Marta Castelli ^{1,*}, Andrea Filipello ², Claudio Fasciano ¹, Giulia Torsello ¹, Stefano Campus ³ and Rocco Pispico ²

¹ Department of Structural, Building and Geotechnical Engineering, Politecnico di Torino, 10129 Turin, Italy; claudio.fasciano@studenti.polito.it (C.F.); giulia.torsello@polito.it (G.T.)

² Agenzia Regionale per la Protezione Ambientale del Piemonte, 10135 Turin, Italy; andrfili@arpa.piemonte.it (A.F.); rocco.pispico@arpa.piemonte.it (R.P.)

³ Regione Piemonte, 10127 Turin, Italy; stefano.campus@regione.piemonte.it

* Correspondence: marta.castelli@polito.it

Abstract: Landslides are a major global threat, endangering lives, infrastructure, and economies. This paper introduces the *Geohazard* plugin, an open-source tool for QGIS, designed to support medium–small-scale landslide analysis and management. The plugin integrates several algorithms, including the *Groundmotion–C index* for evaluating SAR data reliability, *Landslide–Shalstab* for assessing shallow landslide susceptibility, and *Rockfall–Droka* for estimating rockfall invasion areas and the rockfall relative (spatial) hazard. An application example is provided for each module to facilitate validation and discussion. A case study from the Western Italian Alps highlights the practical application of the *Rockfall–Droka* modules, showcasing their potential to identify critical zones by integrating the results on affected areas, process intensity, and preferential paths. Emphasis is given to the calibration of model parameters, a critical aspect of the analysis, achieved through a back-analysis of a rockfall event that occurred in June 2024. The *Geohazard* plugin streamlines geohazard assessments, providing land managers with actionable insights for decision-making and risk mitigation strategies. This user-friendly GIS tool contributes to enhancing resilience in landslide-prone regions.



Academic Editor: Fabrizio Terenzio Gizzi

Received: 18 December 2024

Revised: 23 January 2025

Accepted: 25 January 2025

Published: 30 January 2025

Citation: Castelli, M.; Filipello, A.; Fasciano, C.; Torsello, G.; Campus, S.; Pispico, R. *Geohazard* Plugin: A QGIS Plugin for the Preliminary Analysis of Landslides at Medium–Small Scale. *Land* **2025**, *14*, 290. <https://doi.org/10.3390/land14020290>

Copyright: © 2025 by the authors. Licensee MDPI, Basel, Switzerland. This article is an open access article distributed under the terms and conditions of the Creative Commons Attribution (CC BY) license (<https://creativecommons.org/licenses/by/4.0/>).

Keywords: land management; landslides assessment; open-source; GIS-based tools; *Geohazard* plugin

1. Introduction

Protecting individuals and the environment from hydrogeological risks represents a formidable challenge within the framework of slope stability, particularly rapid over these years of extreme weather events and climate change. Increasing temperatures, permafrost thaw, sea level rise, extreme precipitation events, glacier retreat, changing snowpack dynamics, and an increased frequency of intense storms have significantly increased the likelihood and intensity of catastrophic events such as landslides and floods [1–3]. The risks and damages caused by these catastrophic events are exacerbated by urbanization, infrastructure development, and economic growth in high-risk areas (such as unstable slopes, coastal zones, or flood-prone regions), where the presence of valuable assets (e.g., buildings, infrastructure, and economic resources) and human populations increase their vulnerability to these hazards [4–6]. Within this complex landscape of hydrogeological risk, the interplay of geological, morphological, hydraulic, and climatic factors generates a variety of instability phenomena, each with distinct dynamics, evolutionary characteristics, and spatial impacts [7,8].

The effective management and mitigation of landslide risk require robust tools for danger identification, susceptibility and hazard analysis, and landslide monitoring [9,10]. Modern advancements in remote sensing technologies and Geographic Information Systems (GISs) have become indispensable in this domain, offering powerful data analysis, spatial modeling, and visualization capabilities. Techniques such as satellite-based radar interferometry (InSAR), GPS systems, and sensor networks enable the continuous and detailed observation of slope movements and targets exposed at risk. In particular, InSAR and its variant, Permanent Scatterer InSAR (PSInSAR), have proven invaluable for monitoring slow landslides over extended periods, providing millimeter-level precision in displacement measurements [11–14].

The rate of movement is a key parameter in landslide management, significantly influencing monitoring strategies and risk assessment outcomes. Large, slow movements can be effectively monitored using InSAR techniques, which provide valuable datasets for defining potential landslide scenarios and analyzing landslide behavior. These insights are essential for designing appropriate risk mitigation measures [15]. Conversely, rapid landslides, characterized by sudden instabilities and velocities often exceeding 5 m/s [16], present significant challenges for real-time monitoring. These events are typically widespread, recurrent across extensive areas, and difficult to predict, further complicating data collection and hazard assessment [17]. Thus, rapid and unpredictable events such as rockfalls and earth flows demand preliminary spatial assessments to identify critical zones that warrant detailed studies [18–21]. In this context, GIS-based models have become indispensable tools for territorial analysis, enabling large-scale evaluations based on equivalent parameters. Numerous GIS tools and plugins have been developed for susceptibility and hazard assessments of various landslide types, addressing different aspects.

Regarding slope susceptibility to landslides, models like Stability Index Mapping (SINMAP) [22] evaluate the slope stability by integrating hydrological and geotechnical factors. Similarly, Shallow Landslide Stability (SHALSTAB) [23] integrates topographic attributes with simplified mechanical and hydrological parameters to estimate the shallow landslide potential in relation to rainfall infiltration. To address uncertainties in physically based landslide susceptibility analysis, especially in seismic regions, First-Order Reliability Method (GIS-FORM) provides a user-friendly GIS extension [24]. Meanwhile, Transient Rainfall Infiltration and Grid-Based Regional Slope-Stability (TRIGRS) [25] incorporates transient hydrological inputs in the stability analysis of slopes. The QPROTO plugin [10,21], designed for the QGIS environment, allows preliminary rockfall hazard assessments by estimating the potential invasion area and process intensity based on a set of source points and some equivalent parameters. Finally, open-source GIS tools such as QGIS and GRASS GIS support modular geohazard assessments. For instance, the GRASS GIS module *r.slope.stability* [26] enables physically-based slope stability analyses over extensive areas, integrating datasets, geotechnical parameters, and elevation models. This module provides a flexible framework for assessing the slope failure probability or factor of safety using limit equilibrium methods. Additionally, *r.slopeunits* facilitates reproducible terrain subdivision and classification, enhancing the landslide modelling reliability [27].

However, despite the widespread availability of these methods, their applicability is often restricted to a partial evaluation of the problem. Additionally, their computational intensity and reliance on extensive input data frequently limit their usability, particularly for non-expert users and large-scale applications. Integrating specialized algorithms into user-friendly GIS platforms thus remains challenging, and there is the need to extend accessibility for non-expert users and hinder the practical application of advanced geohazard assessment techniques. The *Geohazard* plugin was developed as an open-source tool within the QGIS environment to address this gap. The *Geohazard* plugin incorporates algorithms

targeting key aspects of slope instability, including an SAR data reliability evaluation, a susceptibility analysis for shallow landslides, and a spatial hazard assessment for rockfall phenomena. Practical applications and case studies demonstrate how the plugin simplifies complex analyses and supports practical decision-making for more resilient and sustainable landscapes in landslide-prone areas. The plugin facilitates efficient and scalable geohazard assessments across varying spatial scales, providing land-use planners, hazard managers, and decision-makers with actionable insights into geohazard identification.

2. Materials and Methods

The *Geohazard* plugin [28] incorporates several specialized algorithms to evaluate the reliability of InSAR data in monitoring slow landslide phenomena, to assess slope susceptibility to shallow landslides, and to perform a preliminary assessment of rockfall spatial hazard. Key algorithms included in the *Geohazard* plugin are the following:

- *Groundmotion–C index*: This algorithm evaluates the reliability of SAR data for monitoring slope movements by calculating the *C index* [29], a parameter that quantifies satellite observation accuracy. The result is a map of the representativeness of InSAR data for slow landslide monitoring, useful for accurate data interpretation in terms of magnitude and velocity of the slope displacements;
- *Landslide–Shalstab*: This algorithm evaluates slope susceptibility to shallow landslide triggering by calculating a critical rainfall infiltration, based on the hydro-mechanical model developed by [23]. The result allows the preliminary identification of areas prone to shallow landslide under different infiltration conditions at a medium/small scale;
- *Rockfall–Droka_Basic* and *Rockfall–Droka_Flow*: These two algorithms estimate zones potentially impacted by rockfall events originating from distributed source points on a slope. The estimation is based on the energy line concept and employs two approaches: *Droka_Basic* utilizes the Cone Method to identify areas that can be reached from one or more rockfall source points [30]; *Droka_Flow* is based on a hydrological model to simulate rockfall trajectories, resembling the path of a water droplet descending along the steepest gradient. Both algorithms provide a spatial representation of rockfall phenomena, including indications of the invasion zone, block velocities, and kinetic energy levels reached in the exposed areas. Such results can provide a preliminary assessment of rockfall susceptibility and relative spatial hazard at a medium–small scale.

2.1. Groundmotion–C Index

The SAR is an active remote sensing technique wherein an antenna emits radiation upon reaching the ground surface and is reflected and captured by the same sensor. SAR data can enable the creation of 3D terrain models; their processing allows monitoring ground deformations and studying landslide phenomena with millimetric precision. Within the Copernicus program [31], data acquired by the Sentinel-1 satellites are freely available through the European Ground Motion Service (EGMS), updated annually. These data support applications such as monitoring the structural integrities of dams, bridges, railways, and buildings. It also allows urban planners to make data-driven decisions regarding infrastructure development by assessing the potential risks posed by natural hazards, such as landslides or subsidence [32].

To facilitate the interpretation of SAR data, the first algorithm within the *Geohazard* plugin calculates the *C index*, an indicator representing the percentage of ground movement detectable by a satellite. The index is important for evaluating the capability of the satellite to monitor ground movements and identify deformations or terrain changes. Additionally,

a visibility percentage map is produced, which is a function of the position of the satellite to the slope, accounting for the radar acquisition angles. The visibility map helps determine the effectiveness of the satellite in collecting accurate and comprehensive data. Finally, the model produces a visibility class map, classifying the terrain into areas according to their visibility (Table 1). This classification provides a detailed overview of areas that can be monitored more precisely than others, aiding in optimizing satellite data usage for planning and monitoring activities.

Table 1. Input and output for the *C index* module.

Input	Format	Description
DTM	Raster	DTM of the area
Cell size	Number	DTM cell size (m)
Track angle φ	Number	Track angle of each measurement point; range (0–360°)
Incidence angle θ	Number	Incidence angle of each measurement point; range (0–90°)
Output	Format	Description
<i>C index</i>	Raster	<i>C index</i> computed in each DTM cell (–1; 1)
Percentage of visibility	Raster	V_{REAL} percentage (0; 100)
Class of visibility	Raster	Classification of V_{REAL} : Class 1: 0–20% Class 2: 20–40% Class 3: 40–60% Class 4: 60–80% Class 5: 80–100%

SAR displacement measurements are one-dimensional, capturing only the movement component along the Line Of Sight (LOS), which is tilted with respect to the vertical at an angle that varies depending on the satellite and the acquisition geometry. In flat terrains and slopes exposed to the north or south, two-dimensional analysis is possible using ascending and descending passes. However, the system exhibits limited sensitivity along the direction of the sensor orbital. Since the orbits of the main satellites (ERS, Sentinel, and RADARSAT) are almost polar, any deformation occurring along the north–south direction results in minimal projection along the LOS. To address this limitation, a correction index *C* can be applied to each LOS measurement to compute the actual velocity component in the slope direction (V_{SLOPE}). The *C index* incorporates satellite-dependent parameters, such as incidence angle θ , i.e., the inclination of the LOS with respect to the vertical, and track angle, i.e., the angle between the projection of the satellite trajectory on the horizontal plane and geographic north. It also accounts for topographic parameters, including ground slope α and aspect β [29,33].

Figure 1 illustrates a geometric overview of the algorithm fundamentals. In Figure 1a, the orientation of the satellite’s orbit and the ground are depicted relative to the geographic north [33]. The angles φ and β represent the azimuth directions (aspect) of the satellite orbit and the ground, respectively. Figure 1b describes the relationship between the satellite’s orbit, the LOS, and the ground, where α is the inclination of the ground, θ is the incidence angle of the LOS relative to the ground, and γ is the angle between the ground and the LOS.

The track and incidence angles are provided within the processed SAR images for each satellite, while slope and aspect values are derived from a DTM. The resolution of the DTM significantly influences the accuracy of the *C index*. High-resolution DTMs improve the representation of terrain profiles but introduce greater variability in slope and aspect values, impacting *C index* computation and subsequent V_{SLOPE} calculations. For balanced accuracy

and computational efficiency, a cell resolution of at least 20 m is recommended, consistent with InSAR data resolution [34]. The *C index* represents the component of movement detectable by the SAR sensor, with a value ranging from -1 to 1 .

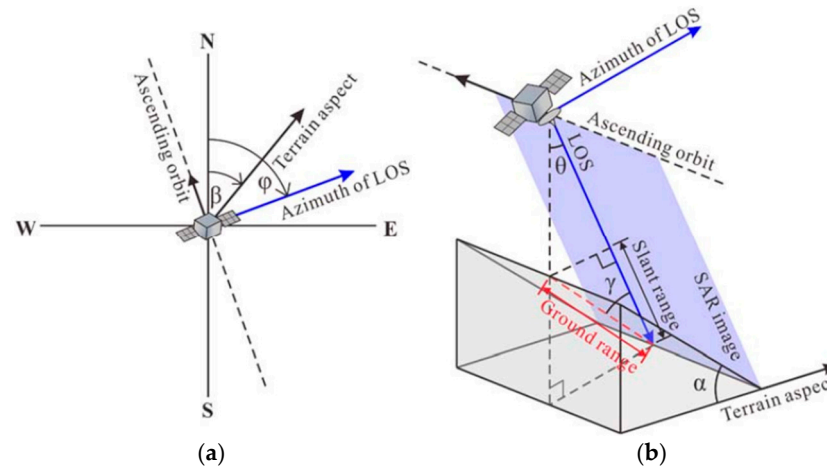


Figure 1. Diagram showing the relationship between LOS parameters of satellite, terrain aspect, and SAR imaging geometry [33]: (a) β is the aspect of the local ground surface (terrain), and φ is the aspect of the LOS; and (b) α is the inclination of the ground, θ is the incidence angle of the LOS, and γ is the angle between the ground and the LOS.

The *C index* is a function of the incidence and track angles and the characteristics of the slope and can be calculated as follows:

$$C = \left[N \cdot \cos(S) \cdot \sin\left(A - \frac{\pi}{2}\right) \right] + \left[E \cdot (-1) \cdot \cos(S) \cdot \cos\left(A - \frac{\pi}{2}\right) \right] + [H \cdot \sin(S)] \quad (1)$$

where S is the slope of the surface; A is the aspect of the surface with respect to north; and N , E , and H are direction cosines [29]. This allows the calculation of V_{SLOPE} (mm/year), the projection of the LOS velocity (V_{LOS}) along the direction of maximum slope, using the following relationship [35,36]:

$$V_{SLOPE} = \frac{V_{LOS}}{C} \quad (2)$$

The relationship also allows for estimating whether the movement is toward or away from the satellite. Indeed, for values of C close to 1 , the satellite accurately observes the movement, and V_{SLOPE} tends to V_{LOS} . For negative C values, the movement is recorded in the reverse direction relative to the LOS geometries. In this case, if the velocity components are consistent with the movement along the slope, V_{SLOPE} will have a sign opposite to V_{LOS} . For values of C close to zero, V_{SLOPE} tends toward infinity, significantly amplifying errors in the projection. Furthermore, it should be noted that positive V_{LOS} values can indicate either potential errors or real movements. When V_{SLOPE} shows a positive value, it may indicate that a landslide is moving upward rather than downward, an unlikely condition. Therefore, such cases should be assessed individually [29].

The processing model in QGIS generates a percentage visibility map that illustrates proportion of the velocity V_{LOS} along the direction of maximum slope. The percentage of visibility is calculated using the formula:

$$\%V_{REAL} = abs(C) \cdot 100 \quad (3)$$

This thematic map helps in quantifying the proportion of the terrain visible to the satellite, accounting for the radar acquisition angles. The visibility percentage serves as a critical metric for assessing the capability of the satellite to acquire accurate and com-

prehensive data. Additionally, the algorithm generates a visibility classification map that categorizes the terrain into five distinct classes based on visibility levels. This classification provides a detailed representation of areas with varying monitoring precision, highlighting regions where data acquisition is more effective.

The calculation of the *C index* has been implemented in the *Geohazard* plugin, and input data and results are shown in Table 1.

Example of Application and Validation of the Model

For each module, a training dataset is provided within the *Geohazard* plugin. Validation and demonstration of results were carried out by applying the *C index* algorithm to the training dataset, related to a high mountain area of $154 \times 172 \text{ m}^2$ in Piemonte (Italy). The DTM used for this analysis has a cell size of 25 m [37] to balance accuracy and computational efficiency. SAR data acquired by the Sentinel-1 satellites [31] were employed with the following orbital parameters: for the ascending orbit, the incidence angle θ was 39° and the track angle ($\varphi + 90^\circ$) was 350° ; and, for the descending orbit, θ remained 39° with ($\varphi + 90^\circ$) set to 190° . Figure 2 illustrates the resulting maps of the *C index* and visibility classes for both ascending and descending orbits. Slopes with higher visibility in the ascending orbit generally exhibit lower visibility in the descending orbit. Areas where the *C index* approaches 1 or -1 (indicated as darker green zones in Figure 2a,b) correspond to regions where V_{LOS} closely approximates V_{REAL} , aligning with high-visibility classes (Figure 2c,d). Conversely, areas where the *C index* is near 0 (white zones in Figure 2a,b) correspond to low-visibility classes (Figure 2c,d). Class 5 denotes regions with nearly 100% visibility, where satellite-detected displacement V_{LOS} closely matches actual ground movement V_{REAL} . In contrast, class 1 identifies areas with very low visibility, where interpretation of displacement and velocity measurements require greater caution. These results indicate the reliability of satellite data for detecting ground displacements and highlight their utility in small-to-medium-scale land-monitoring activities, enabling the comparison of displacements across areas and the identification of slow slope movements.

To validate the calculations made by the algorithm, an Excel spreadsheet was created, incorporating Equation (1) to derive the *C index* based on ground aspect β and slope α from the DTM, and incidence angle θ and track angle ($\varphi + 90^\circ$) from the orbital parameters. A comparison between the external Excel calculations and the results of the algorithm was conducted on nine cells, with three cells selected for each pair of incidence and track angles. The results confirmed the validity and accuracy of the model, as summarized in Table 2.

Table 2. Comparison of results for *C index* validation.

Aspect β ($^\circ$)	Slope α ($^\circ$)	Incidence Angle θ ($^\circ$)	Track Angle $\varphi + 90$ ($^\circ$)	<i>C index</i> (Excel)	<i>C index</i> (Model)
79	15	39	350	0.81	0.81
291	39	39	350	0.04	0.03
252	11	39	350	-0.46	-0.47
159	22	35	310	0.05	0.04
43	48	35	310	0.99	0.99
118	41	35	310	0.63	0.62
133	35	37	330	0.60	0.60
243	12	37	330	-0.42	-0.42
260	24	37	330	-0.19	-0.19

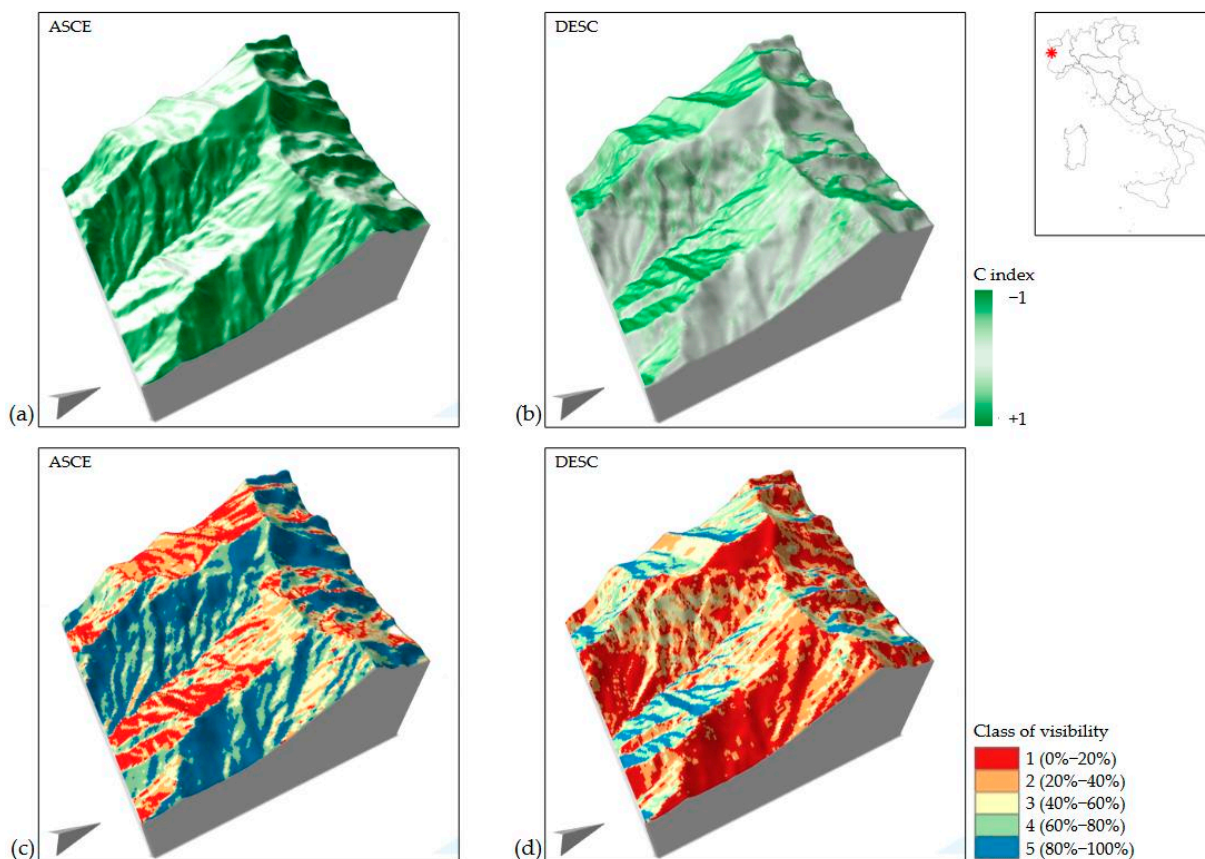


Figure 2. Example of application of the *Groundmotion–C index* algorithm (DTM 25 m, Sentinel-1): (a) *C index* map in ascending orbit; (b) *C index* map in descending orbit; (c) class of visibility map in ascending orbit; and (d) class of visibility map in descending orbit.

2.2. Landslide–Shalstab

Shalstab is a physically-based model used to assess the triggering of shallow landslides due to infiltrated rainfall, following the method proposed by [23,38]. The method (Figure 3) enables the analysis of topographic, soil, and rainfall data to evaluate slope stability and solves the relevant equations using a gridded terrain representation, combining a limit equilibrium stability model for infinite slopes with a steady-state hydrological model. The main assumptions underlying the formulation are as follows [39,40]:

- Infinite slope;
- Planar failure surface, parallel to the slope, located at the interface between the shallow layer and the underlying layer of lower permeability;
- Mohr–Coulomb shear strength criterion expressed in terms of effective stresses;
- Steady flow parallel to the slope;
- Absence of deep drainage and flow within the underlying substrate.

According to the Limit Equilibrium Method, the stability condition is determined by calculating the Factor of Safety (Figure 3a and Equation (4)):

$$F_S = \frac{c' + (\gamma \cdot z \cdot \cos^2\theta - u) \cdot \tan\phi'}{\gamma \cdot z \cdot \sin\theta \cdot \cos\theta} \tag{4}$$

$$u = \gamma_w \cdot h \cdot \cos^2\theta \tag{5}$$

where θ is the slope inclination, z is the landslide thickness, c' and ϕ' are cohesion and friction angle, respectively, γ is soil unit weight, u is water pressure on the failure surface, γ_w is water unit weight, and h is the water table level above the failure plane.

There are several approaches to considering the effects of rainfall and its infiltration into the soil. In *Shalstab*, steady-state conditions are assumed, meaning there is no temporal variation in rainfall and soil saturation. The model is based on the observation that shallow landslides tend to occur in topographic hollows, where shallow subsurface flow convergence leads to increased soil saturation, pore pressure, and reduced shear strength, thus triggering potential failure. The hydrological component of the model is simplified by assuming that rainfall infiltrates the soil and is routed downslope, following the topographic gradient. This implies that the contributing area at any given point is defined by the specific catchment area derived from the surface topography (Figure 3b). For a detailed analytical discussion of the hydrological model employed in *Shalstab*, reference can be made to [38,39].

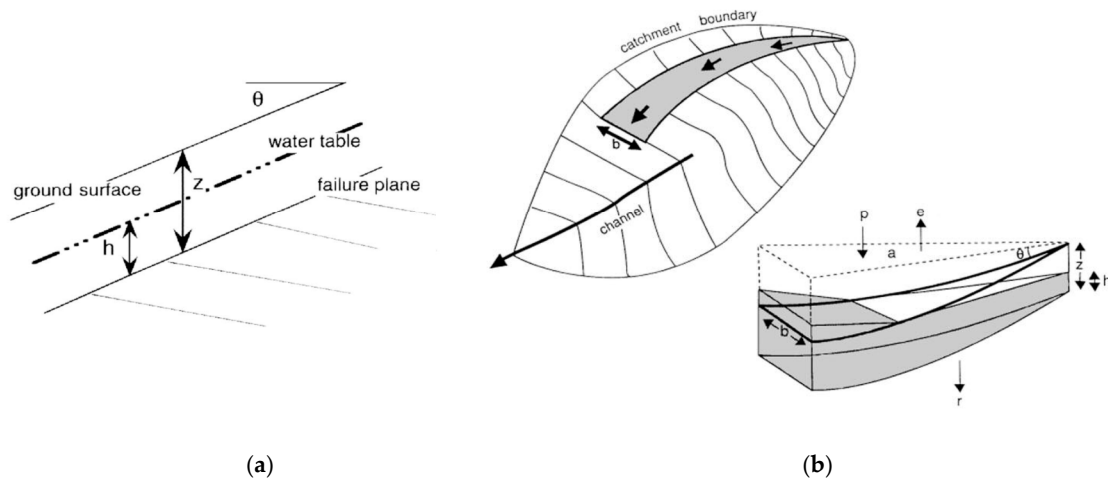


Figure 3. The hydro-mechanical model underlying the *Shalstab* module [39]: (a) infinite slope model, where z is the thickness of the shallow layer, h is the height of the saturated layer above the failure surface, and θ is the inclination of the slope; and (b) geometry of the catchment and flow path of water in the hydrological model, where a is the contributing upslope area draining across the contour length b .

The following section outlines the hydrologic component of this model that, coupled with the stability component (Equations (4) and (5)), leads to the implementation of the F_S equation (Equation (6)):

$$F_S = \frac{c' + (-W \cdot \gamma_w) \cdot z \cdot \cos^2 \theta \cdot \tan \phi'}{\gamma \cdot z \cdot \sin \theta \cdot \cos \theta} \tag{6}$$

The instability condition ($F_S \leq 1$) for each cell in the domain is expressed by Equation (7):

$$\frac{a}{b} \geq \left[\frac{c'}{\gamma_w \cdot z \cdot \sin \theta \cdot \cos \theta} + \frac{\gamma}{\gamma_w} \cdot \left(1 - \frac{\tan \theta}{\tan \phi'} \right) \right] \cdot \frac{T}{q} \cdot \sin \theta \tag{7}$$

where, according to Figure 3b:

- a is the contributing upslope area draining across the contour length b ;
- $T = K_s \cdot z \cdot \cos \theta$ and K_s is the permeability coefficient of saturated soil;
- $W = \frac{h}{z} = \frac{q}{T} \cdot \frac{a}{b \cdot \sin \theta}$ and q is effective rainfall.

This condition is evaluated only for cells that do not meet the conditions of absolute stability and absolute instability, given by the following:

$$\tan \theta \leq \left(1 - \frac{\gamma_w}{\gamma} \right) \cdot \tan \phi' \quad (\text{absolute stability}) \tag{8}$$

$$\tan\theta \geq \frac{c'}{\gamma_w \cdot z \cdot \cos^2\theta} + \tan\phi' \quad (\text{absolute instability}) \tag{9}$$

The condition of absolute stability identifies cells classified as stable even when the soil is fully saturated. The condition of absolute instability indicates cells that are unstable even in the absence of infiltration.

Furthermore, by imposing the limit equilibrium condition ($F_S = 1$) and solving Equation (7) with respect to q , the critical infiltration q_{cr} threshold can be determined (Equation (10)):

$$q_{cr} = \left[\frac{c'}{\gamma_w \cdot z \cdot \sin\theta \cdot \cos\theta} + \frac{\gamma}{\gamma_w} \cdot \left(1 - \frac{\tan\theta}{\tan\phi'} \right) \right] \cdot \frac{a}{b} \cdot T \tag{10}$$

If the information on the presence of roots in the shallow soil layers is available, their resistance contribution can be incorporated by increasing the soil cohesion, which will then be composed by the sum of the contribution of soil c_{soil} and roots c_{root} .

Based on the aforementioned method, the *Shalstab* algorithm provides the spatial distribution of the absolute stable and absolute unstable cells, as well as the critical effective (infiltrated) rainfall that leads each cell to a F_S of 1. The required input data are listed in Table 3. Although most parameters vary spatially across the slope, to assist the user in preparing a quick analysis, the *Geohazard* plugin includes an additional tool called *Shalstab input raster creator*, which allows for the generation of constant-value input raster files from the DTM.

Table 3. Input for the *Shalstab* module.

Input	Format	Description
DTM	Raster	DTM of the area
Cell size	Number	DTM cell size (m)
Depth z	Raster	Thickness of the potentially unstable layer (m)
Unit weight γ	Raster	Soil unit weight (N/m^3)
Friction angle ϕ'	Raster	Soil friction angle ($^\circ$)
Permeability K_s	Raster	Soil permeability coefficient (m/h)
Soil cohesion c_{soil}	Raster	Soil cohesion (N/m^2)
Root cohesion c_{root}	Raster	Root cohesion (N/m^2)

The results of the analysis are given as 4 raster maps, showing the following: (1) absolute stable zones; (2) absolute unstable zones; (3) distribution of critical infiltrated rainfall q_{cr} (mm/day); and (4) susceptibility classes. In the q_{cr} map, absolute stable cells assume no data values and absolute unstable cells assume $q_{cr} = 0$. The susceptibility raster map is a reclassification of q_{cr} in 7 classes (Table 4) as suggested by [38]. This classification provides the value of q_{cr}/T in logarithmic form. This ratio reflects the magnitude of the water infiltration, represented by q , concerning the ability of the surface to move the water downslope, i.e., the transmissivity (T). The larger the value of q relative to T , the more likely the ground is to become saturated. This is a useful representation for identifying areas of the study domain with different behaviour and it can be interpreted as a susceptibility map since it spatially classifies the distribution of instability conditions. It can be converted into a hazard map if an infiltration model is applied, to compute a critical triggering gross rainfall P_{cr} from q_{cr} . Given P_{cr} , the probability of occurrence of the related meteorological event can be made explicit as a return period and the time dimension of hazard is achieved [41].

Table 4. Susceptibility classes.

Class	$\log(q_{cr}/T)$ (1/m)	
1	−inf	−3.4
2	−3.4	−3.1
3	−3.1	−2.8
4	−2.8	−2.5
5	−2.5	−2.2
6	−2.2	−1.9
7	−1.9	+inf

Example of Application and Validation of the Model

To demonstrate the results on a small scale and validate the calculations, the *Shalstab* module was applied to the Deago area, a region of approximately 400 km² located in the hilly Langhe region, northwestern Italy. This area corresponds to sheet 211 of the Italian 1:50,000 map series produced by the Italian Cartographic Authority (IGM). The Deago area was previously analyzed as part of the Carg Project [42], which aimed to produce thematic geological maps of the Italian territory. In the Carg Project, absolute hazard was defined by incorporating the temporal component, represented by the return period of critical rainfall, and the assessment of the destructive potential of landslide phenomena (intensity). For validation purposes, the *Shalstab* module utilized input data derived from the Carg Project (Table 5), obtained through a detailed analysis of parameter variability within the Deago area. The results obtained in terms of absolute stable, absolute unstable cells, and distribution of q_{cr} were compared.

Table 5. Input parameters used for the validation on the Deago area.

Input	Value
DTM	[37]
Cell size	10 m
Depth z	0.52–1.09 m
Unit weight γ	22,000 N/m ³
Friction angle φ'	24–32°
Permeability K_s	0.144 m/h
Soil and root cohesion c	20,000–35,000 N/m ²

In Figure 4a, the resulting critical rainfall map (q_{cr}) is shown after applying the *Shalstab* model to the Deago area. Twenty representative cells in different areas were considered for comparison (Table 6): the values of critical infiltration vary with negligible differences, due to the use of different hydrology calculation algorithms. However, this comparison highlights the accuracy of the obtained results, and the validation can be considered successful. In Figure 4b, the results are presented for a specific portion of the study area (highlighted as a zoomed-in region in Figure 4a), and compared against the inventory of shallow landslides triggered during the November 1994 rainfall event. This comparison provides additional qualitative validation of the model, particularly given that the cumulative daily rainfall in this region exceeded 200 mm/day during the event, corresponding to a return period of approximately 100 years.

To evaluate the influence of DTM cell size on the analysis results, the calculation was repeated for the same area using the DTM 5 m provided by Regione Piemonte [37]. The parameters listed in Table 5 were used for consistency. Table 7 reports the critical rainfall q_{cr} values for the 20 representative points derived from the analyses using both 10 m and 5 m DTMs.

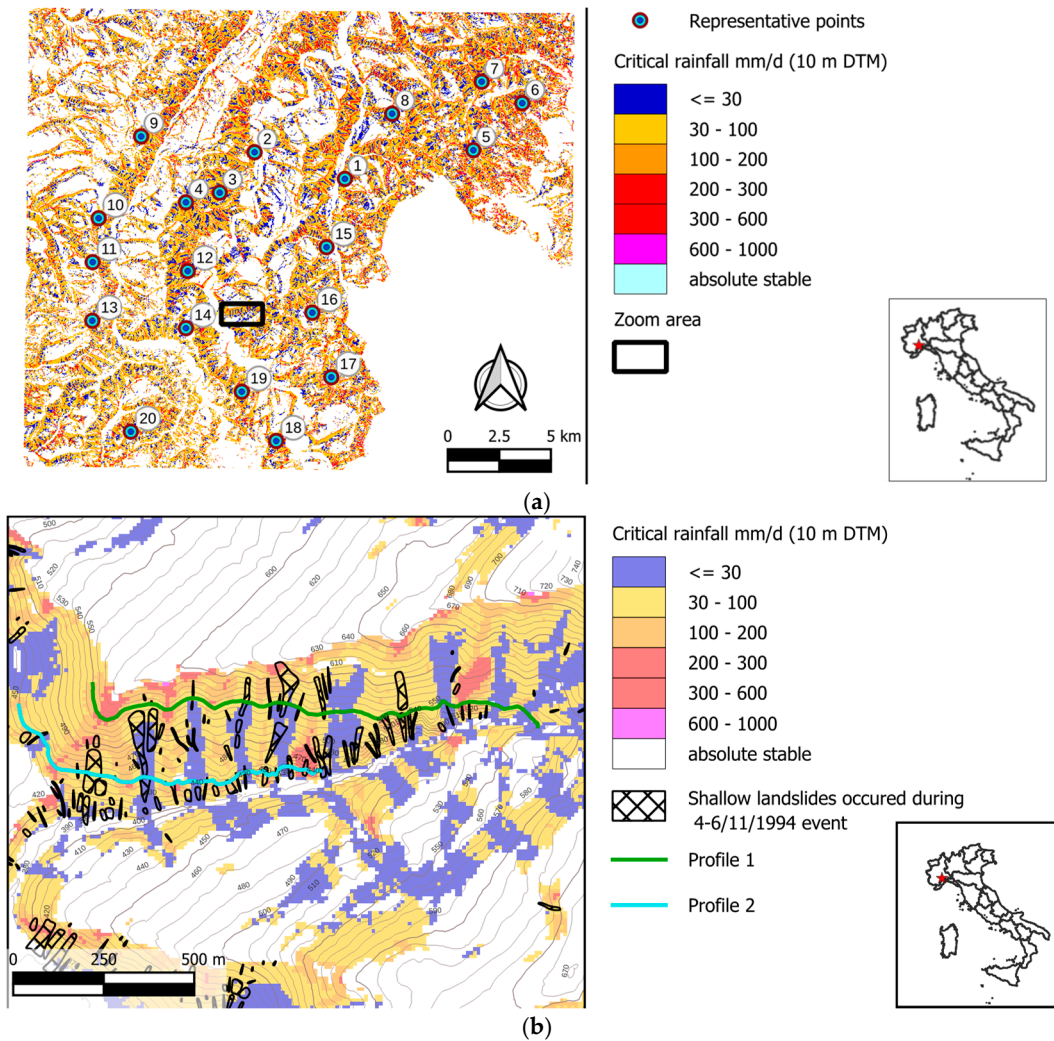


Figure 4. Results of the application of the *Shalstab* module to the Dego area: (a) critical infiltrated rainfall q_{cr} computed across the entire area using a DTM 10 m, with the zoomed-in region and validation points indicated (refer to Tables 6 and 7); and (b) zoomed-in area, highlighting the shallow landslides triggered during the November 1994 heavy rainfall event, as well as profile 1 and profile 2 used to compare the results obtained with different DTM resolutions (Figure 5).

For comparison, the difference between the q_{cr} values and the corresponding susceptibility classes are included. An additional comparison is given through the profiles illustrated in Figure 4b, which represent two contour lines located at 450 m (profile 1) and 550 m (profile 2). The q_{cr} values along these profiles, obtained from their intersection with the respective maps (based on DTM 10 m and DTM 5 m), are shown in Figure 5. The results indicate that the difference in q_{cr} calculation between DTMs can be significant, particularly in areas where the slope is not uniform. This discrepancy is probably due to the influence of DTM resolution on both the mechanical stability factor F_s and the hydrological component of the model. Variations in slope inclination and catchment area calculations across cells are directly affected by the DTM resolution. These differences affect the susceptibility classification of the area, highlighting the importance of DTM resolution in such analyses. This aspect, which has implications for model accuracy and reliability, will be further investigated in future studies.

Table 6. Validation of the *Shalstab* module via comparison with the Carg project.

ID	q_{cr} <i>Shalstab</i> (mm/day)	q_{cr} Carg (mm/day)	Difference (mm/day)
1	39.04	37.04	−2.00
2	56.13	57.87	−1.74
3	87.76	88.45	−0.69
4	62.68	63.34	−0.66
5	117.52	116.64	0.88
6	37.49	40.90	−3.41
7	87.33	90.57	−3.24
8	61.82	63.12	−1.30
9	19.33	24.70	−5.37
10	216.83	211.98	4.85
11	167.18	164.83	2.35
12	66.49	68.53	−2.04
13	No data	No data	No data
14	77.45	81.81	−4.36
15	146.66	143.79	2.87
16	198.60	190.48	8.12
17	40.20	42.33	−2.13
18	18.89	18.87	0.02
19	3.98	1.76	2.22
20	40.67	40.08	0.59

Table 7. Validation of the *Shalstab* module on different DTMs.

ID	DTM 10 m		DTM 5 m		Difference $q_{cr,5}-q_{cr,10}$ (mm/day)
	$q_{cr,10}$ (mm/day)	Class	$q_{cr,5}$ (mm/day)	Class	
1	39.04	1	112.02	1	72.98
2	56.13	1	52.74	1	−3.39
3	87.76	2	96.64	3	8.88
4	62.68	1	54.19	1	−8.49
5	117.52	3	334.85	7	217.33
6	37.49	1	No data	-	No data
7	87.33	1	352.74	3	265.41
8	61.82	1	84.97	2	23.15
9	19.33	1	0.55	1	−18.78
10	216.83	6	140.22	4	−76.61
11	167.18	3	103.28	2	−63.9
12	66.49	1	124.89	1	58.4
13	No data	-	No data	-	No data
14	77.45	2	80.96	2	3.51
15	146.66	3	173.97	3	27.31
16	198.60	5	285.56	7	86.96
17	40.20	1	77.27	2	37.07
18	18.89	1	13.31	1	−5.58
19	3.98	1	2.43	1	−1.55
20	40.67	1	27.41	1	−13.26

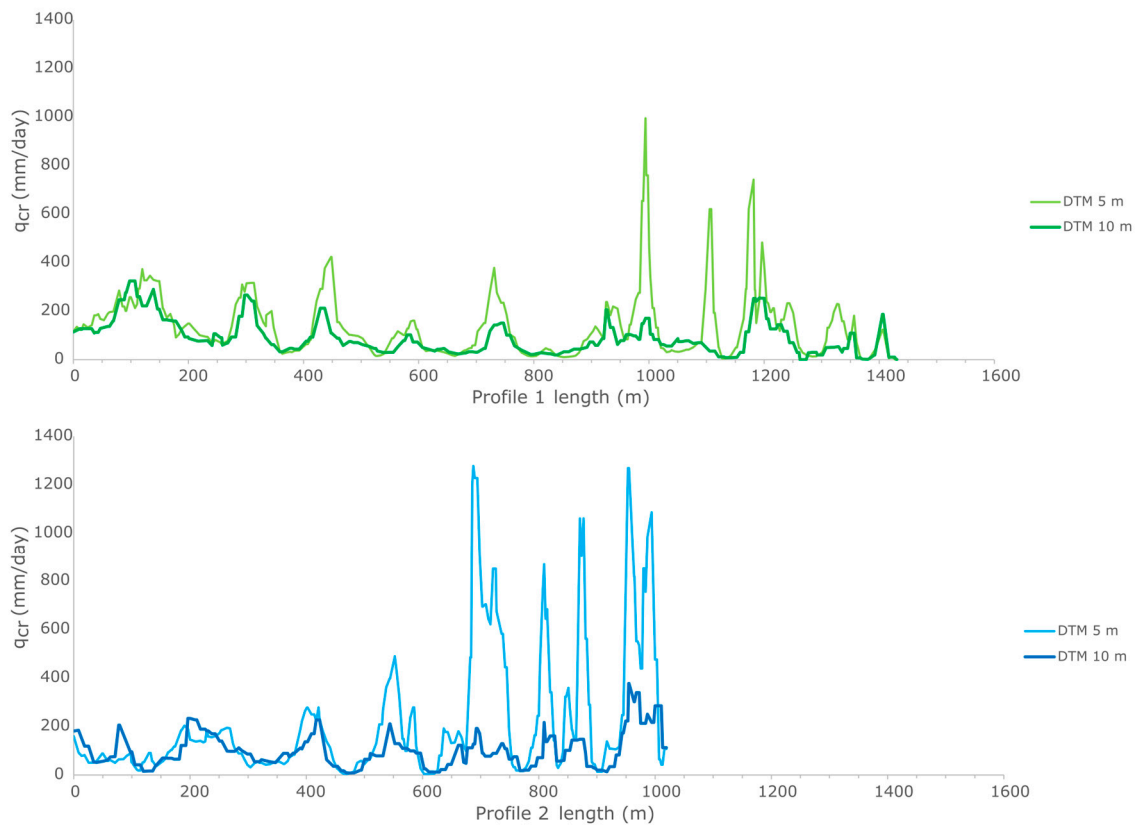


Figure 5. Comparison between the critical infiltrated rainfall q_{cr} computed along profile 1 and profile 2 as depicted in Figure 4b, analyzed using different DTM resolutions.

2.3. Rockfall–Droka

The *Droka* model is devoted to the simplified analysis of rockfall runout from diffuse source points across a slope. The analysis is based on the concept of energy line, the line connecting a rockfall source point to the farthest stopping point of a block detached from that source. The energy line is inclined at an angle φ_p with respect to the horizontal plane (i.e., the energy angle), which can be interpreted as a global block-slope friction angle. This angle is representative of all the dissipative phenomena occurring throughout the motion phases of the block along the slope. The concept of energy line is implemented in the *Geohazard* plugin through two independent, yet complementary, algorithms: *Droka_Basic* and *Droka_Flow*. Both simulations provide results in the form of point vectors, distributed across the invasion zone. For each point, the following information is provided: minimum, maximum, and mean block velocity [m/s]; minimum, maximum, and mean kinetic energy [kJ]; and the number of simulations that affected a specific point (frequency).

The two models use different methods to identify the areas involved in the phenomenon and can be used independently or combined to obtain complementary information. A detailed description of the algorithms is provided below along with a discussion of their potential and limitations through practical application examples.

2.3.1. Rockfall–Droka_Basic

Droka_Basic module is based on the Cone method [10,21,30], which enables the definition of the area affected by rockfall events on a slope. This is achieved through a cone representing the envelope of all possible rockfall paths. The apex of the cone is located at the source point and its geometry is defined by three angles (Figure 6a): the dip direction angle θ of the slope at the source point defines the orientation of the cone; and the energy angle φ_p outlines its vertical extension and the lateral spreading angle α delineates the

extension of the cone in the horizontal plane. The intersection of the cone with the surface of the slope defines the rockfall-affected area, where each point within this area may potentially be reached by a rockfall path originating from the source. When multiple source points are considered, the module can delineate zones subjected to rockfalls through the overlapping of simulated cones. This approach enables the creation of a frequency map, where areas with higher frequencies are the most prone to be reached by fallen blocks, identifying them as the most susceptible to this type of danger. Using the concept of the energy line, the module enables the calculation of the velocity and kinetic energy of the block at any position within the affected area [21]:

$$v(x, y) = \sqrt{2g \cdot \left[H(x_0, y_0) - h(x, y) - \sqrt{(x - x_0)^2 + (y - y_0)^2} \cdot \tan \varphi_p \right]} \quad (11)$$

where g is gravity acceleration, (x_0, y_0) are the source point coordinates, $H(x_0, y_0)$ is the elevation of the source point, $h(x, y)$ is the elevation of the topographic surface in the point (x, y) , and φ_p is the energy angle.

Therefore, the kinetic energy E can be estimated at any position given the block mass m :

$$E(x, y) = \frac{1}{2} \cdot m \cdot v^2(x, y) \quad (12)$$

The Cone method in the *Droka_Basic* module is implemented by constructing a triangle with its apex at each source point, characterized by specified input parameters. A point layer is then generated, containing one point for each DTM cell covered by the triangle. For each point, the height difference ΔH between the ground and the energy line is computed ($\Delta H = h_k(x, y)$, Figure 6a). Points showing a positive ΔH value are identified as part of the invasion area. Starting from ΔH , block velocity and kinetic energy are computed for each point according to Equations (11) and (12).

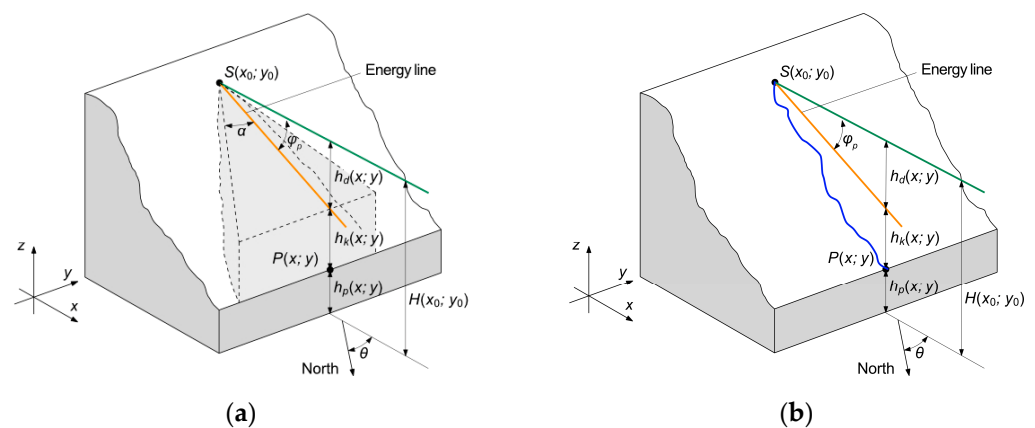


Figure 6. Invasion zone definition and associated geometrical components in the *Droka* modules: (a) *Droka_Basic* representation of the cone with the apex in the source point $S(x_0, y_0)$ and geometry defined by the angles θ , α , and φ_p (in light grey). The cone is sectioned by a vertical plane passing through the generic topographic point $P(x, y)$. The orange line represents the energy line. The horizontal dark green line refers to the total energy of the block. (b) *Droka_Flow* representation of the rockfall path (blue line) originated from the source point S , sectioned by a vertical plane passing through the generic topographic point $P(x, y)$.

The input data required by the *Droka_Basic* module are described in Table 8. The attributes of source points are obtained from the DTM, while the cone parameters are constant across all source points and are specific to each case study. Calibrating these parameters is essential in order to achieve reliable and conservative results. It should be

based on information from past events in the area, rockfall inventories, territorial databases, and quick field observations of the slope. The output is a vector layer of points located at the center of the DTM cells within the affected area, containing the data listed in Table 8.

Table 8. Input and output for the *Droka_Basic* module.

Input	Format	Description
DTM	Raster	DTM of the area
Cell size	Number	DTM cell size (m)
Source points	Point vector layer	Selected source points
Mass m	Number	Block mass (kg)
Energy angle φ_p	Number	Energy angle ($^\circ$)
Lateral spreading angle α	Number	Lateral spreading angle ($^\circ$)
Output	Format	Description
Fid, ID	Number	Points identification
Count	Number	Number of overlapped cones
Energy_min, max, mean	Number	Minimum, maximum, mean kinetic energy (kJ)
Velocity_min, max, mean	Number	Minimum, maximum, mean velocity (m/s)
Percent	Number	Number of overlapping cones at the point as a proportion of the total number of generated cones

2.3.2. Rockfall–Droka_Flow

The *Droka_Flow* module employs a hydrological approach to simulate potential rockfall paths by tracing the line of maximum slope for each source point. The path terminates when the inclination of the line passing through the source point is lower than the inclination of the energy line, defined by the user.

Each analysis includes five simulations from each source point. These simulations adjust DTM elevation using a Monte Carlo approach within a user-defined standard deviation around the original DTM elevation values, assuming a simplified normal distribution of elevation for each cell. The mean corresponds to the original DTM height, while the user-defined standard deviation is constant across cells. This approach provides a simplified representation of the variability in rockfall trajectories due to factors like ground impact, bouncing, and obstacles (e.g., rocks, trees, or structures).

Assuming that the rockfall trajectory remains in constant contact with the ground and follows the steepest downhill gradient, the *Droka_Flow* module employs the GRASS GIS hydrological function *r.drain* to compute five paths from each source point. Starting from a user-defined input point or set of points, the algorithm calculates path directions by evaluating the elevation differences between adjacent cells. The output is a raster map delineating the calculated flow paths. Further details on the methodology and implementation are provided in [43]. As with *Droka_Basic*, the analysis result is a vector point layer, which is then generated, containing one point for each DTM cell covered by the simulated paths. The height difference ΔH between the energy line and the ground is calculated for each point, leading to block velocity and kinetic energy calculations when ΔH is positive (Equations (11) and (12); Figure 6b). The paths are then merged for the statistical analysis of block velocity and kinetic energies.

The input data required by the *Droka_Flow* module are described in Table 9. Once more, source points are obtained from the DTM while the energy angle and the standard deviation of the distribution of cells elevation are specific to each case study. In particular, the standard deviation should be related to the DTM size, as discussed in Section 3. The

output is a vector layer with point attributes similar to those described in *Droka_Basic* and listed in Table 8. Frequency data are omitted here due to the limited number of paths per source point, so energy count and percent fields are not included.

Table 9. Input for the *Droka_Flow* module.

Input	Format	Description
DTM	Raster	DTM of the area
Cell size	Number	DTM cell size (m)
Source points	Point vector layer	Selected source points
Mass m	Number	Block mass (kg)
Energy angle φ_p	Number	Energy angle ($^\circ$)
Mean of the normal distribution	Number	Height difference from DTM (m)
Standard deviation	Number	Standard deviation of the normal distribution of DTM elevation (m)

2.3.3. Validation of the Modules

To validate the results produced by the algorithms implemented in *Droka_Basic* and *Droka_Flow* modules, an initial set of analyses was carried out on a synthetic slope DTM with 5 m cell size. The slope was generated by joining two planar surfaces: a runout plane inclined at 60° to the horizontal and a nearly horizontal plane with an inclination of approximately 2° . A single rockfall source point was located at an elevation of approximately 500 m, with a mass of 2600 kg and a volume of 1 m^3 . Parametric analyses were performed on this synthetic slope to assess the influence of key parameters on the results, using both *Droka_Basic* and *Droka_Flow*. The best parameter fit for both *Droka* modules was found to be lateral spreading angle α equal to 10° , and standard deviation equal to 0.1 m. The results are consistent for the modules, as reported in Figure 7, and align with the simplified analytical model in the calculation of block velocity and kinetic energy, following Equations (11) and (12).

However, for natural slopes, where both aspect and inclination vary widely, rockfall trajectories may spread much more. In addition, natural slopes feature niches, incisions, or debris accumulations due to erosion and instability phenomena over time, which significantly influence the rockfall paths. Therefore, it is suggested to calibrate the parameters for susceptibility analysis to the specific site conditions. A proper calibration can be achieved through the back-analysis of actual events, using data gathered from in situ observations, as described in Section 3.

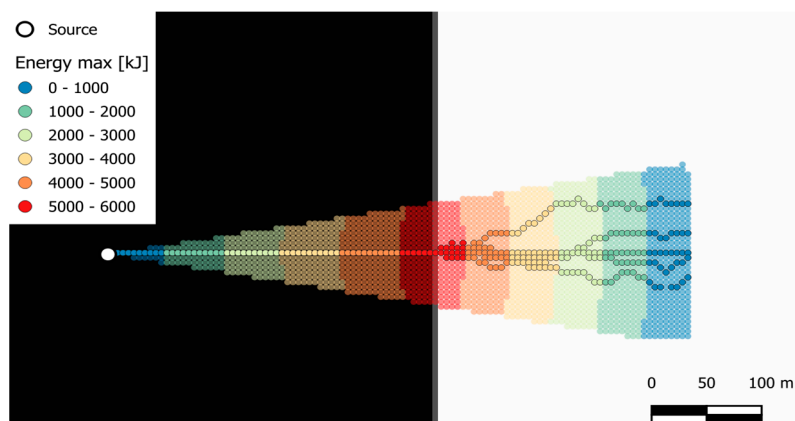


Figure 7. Invasion area and block kinetic energy for the synthetic slope obtained with *Droka_Basic* and *Droka_Flow*. Calibrated parameters are φ_p : 45° , α : 10° , and standard deviation: 0.1 m.

3. Results

This section presents an example of the application of the *Rockfall–Droka* modules for a preliminary assessment of rockfall susceptibility and relative spatial hazard, illustrating the recommended procedure and discussing the results. The example focuses on a steep slope near the village of Bobbio Pellice, Piemonte (Western Alps), where recurrent rockfall events threaten a cluster of alpine buildings. On 24 June 2024, a large rockfall event destroyed one of these buildings, creating high-risk conditions.

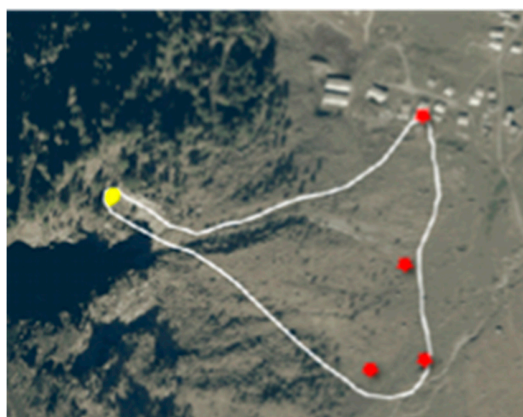
3.1. Parameter Calibration

The Bobbio Pellice rockfall event involved a slope sector impacted by similar events in the past and was triggered by intense meteorological conditions. Observations from the survey conducted by GeoAlpi Consulting (2024) [44] include the following:

- The detachment occurred at approximately 1940 m a.s.l.;
- A block of approximately 30 m³ struck and destroyed a building located at about 1750 m a.s.l., with visible traces along its trajectory (Figure 8a,c);
- This path was influenced by other blocks and debris on the slope, displaced during all the collapses;
- Additional smaller blocks of approximately 1–2 m³ reached the bottom of the valley, with clearly defined trajectories. The stopping position of some of these blocks is shown in Figure 8b.



(a)



(b)



(c)

Figure 8. Bobbio Pellice rockfall event, 24 June 2024: (a) destroyed building; (b) involved area and some stopped blocks on the slope, in red—assumed source area in yellow; and (c) block path reaching the destroyed building, after [44].

Based on the available information, a back-analysis was conducted by selecting three source points located within the steepest area of the involved zone (Figure 8b). A block with a volume of 30 m^3 , mass of $78,000 \text{ kg}$, and unit weight of 2600 kN/m^3 was used to estimate the kinetic energy. The analysis utilized a 5 m resolution DTM provided by Regione Piemonte [37] for an initial set of simulations aimed at parameter calibration and a comparison of results between the *Droka_Basic* and *Droka_Flow* modules.

For *Droka_Basic*, the optimal results in terms of the invasion area were achieved with a lateral spreading angle α of 22° and an energy angle φ_p of 37° , as shown in Figure 9, where the distribution of block kinetic energy within the invasion area is also included. The computed kinetic energy at the impact point with the building is approximately 5000 kJ , consistent with the destruction of the building.

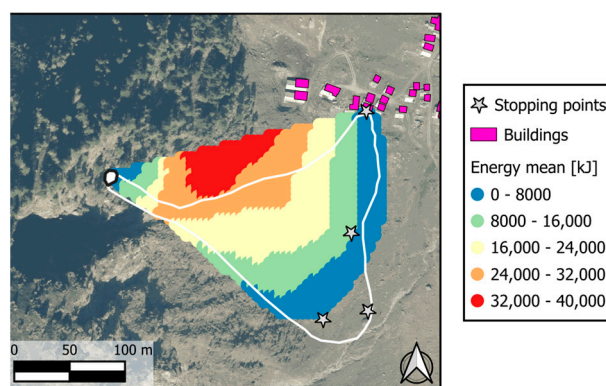


Figure 9. *Droka_Basic* results for the kinetic energy of the back-analysis of the rockfall event. Calibrated parameters are $\varphi_p: 37^\circ$ and $\alpha: 22^\circ$.

To calibrate the *Droka_Flow* model, the influence of the assumed standard deviation was analyzed in this study through a parametric analysis, with standard deviation values ranging from 0.1 m to 5 m (2% to 100% of the DTM cell size). Each simulation was repeated five times to generate about 20 paths (Figure 10). The results suggest that the most conservative simulations occur with standard deviations of 0.5 m and 1 m , corresponding to 10% and 20% of the 5 m DTM cell size, respectively. In these cases, at least one trajectory reaches the affected building, with kinetic energy around 5000 kJ , consistent with the results from *Droka_Basic*. As shown in Figure 10, the simulated paths do not encompass the entire invasion area (in white), as only trajectories in the direction of maximum slope are simulated by the *r.drain* function. Nonetheless, this analysis demonstrates that the location of the building is the most prone to being impacted by a block detached from the source area, indicating it as the most critical area. The combination of *Droka_Flow* and *Droka_Basic* provides dual insights: first, it identifies the entire area potentially impacted by the rockfall, accounting for all possible trajectories, including the less probable ones; and, second, it highlights the most critical paths within this area.

The back-analyses with *Droka_Basic* and *Droka_Flow* modules were repeated with 1 m , (available at the Geoportal of the Italian Ministry of the Environment [45]), 5 m , and 10 m DTM resolutions [37] for evaluating the influence of DTM resolution on the results. Figure 11 shows the results of *Droka_Basic* for the case with $\varphi_p = 37^\circ$ and $\alpha = 22^\circ$. It is worth noting that changes in DTM discretization slightly affect the orientation of source points. Specifically, the 1 m DTM results in a greater variability in the dip direction at the source points compared to the 5 m and 10 m DTMs, leading to a wider invasion area. Despite this variability, a lateral spreading angle α of 22° remains the best calibration to cover the invasion area conservatively. In contrast, with the 10 m DTM, a conservative outcome requires increasing the α value. The optimal φ_p value for delineating the rockfall-affected

area (37°) remains consistent across DTMs, suggesting it is a characteristic parameter of the phenomenon, dependent on the slope geometry and block properties rather than on the DTM resolution. Figure 12 presents the results of *Droka_Flow* for the case with $\varphi_p = 37^\circ$ and a standard deviation of 10% of the DTM size (i.e., 0.1, 0.5, and 1 m for DTM sizes of 1, 5, and 10 m, respectively), which yielded the most conservative results. This comparison shows that the 1 m DTM results in a very limited trajectory spread around the maximum slope path (this result is obtained regardless of the chosen standard deviation). The widest trajectory spread occurs with the 10 m DTM; however, many trajectories fall outside the designated rockfall invasion zone (shown in white in Figure 12). The analysis that better simulates the actual invasion area seems to be with the 5 m DTM, for both *Rockall–Droka* modules.

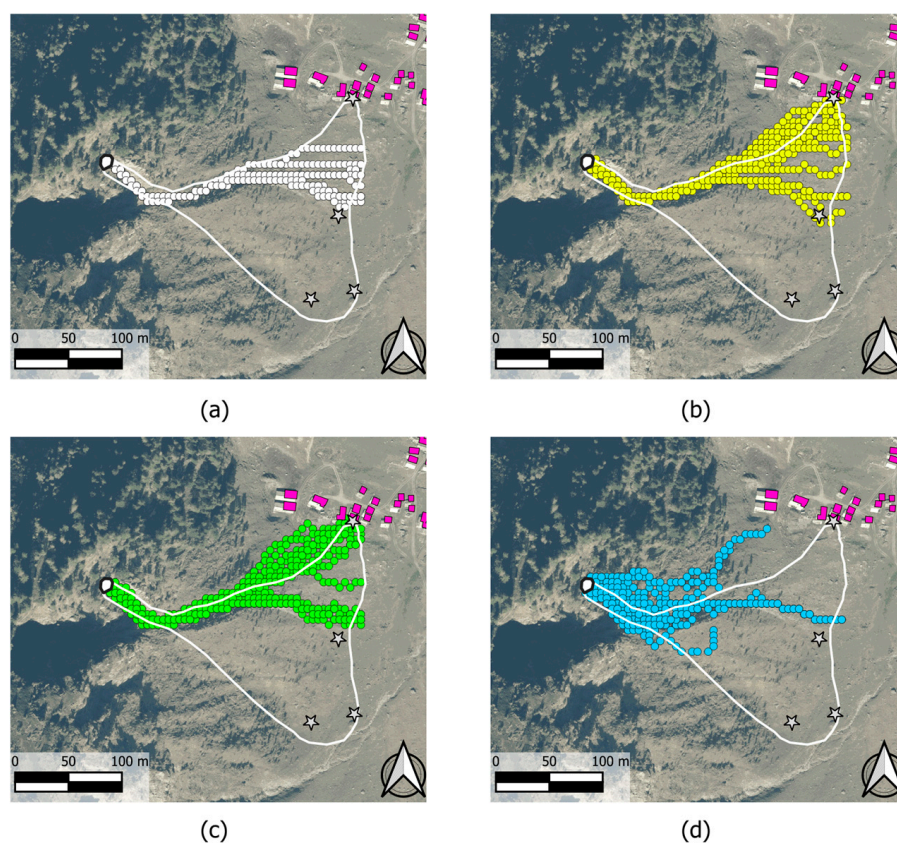


Figure 10. *Droka_Flow* results of the back-analysis of the rockfall event, influence of standard deviation: (a) standard deviation: 0.1 m; (b) standard deviation: 0.5 m; (c) standard deviation: 1 m; and (d) standard deviation: 5 m.

These observations suggest that effective parameter calibration for the susceptibility and hazard analysis can be achieved through the back-analysis conducted within the same geomorphological context and using the same DTM resolution, ensuring consistent results. As discussed, the *Droka_Basic* and *Droka_Flow* modules complement each other, with their comparison highlighting both the most significant trajectories and the full invasion area. This combined approach offers valuable insights for defining rockfall susceptibility.

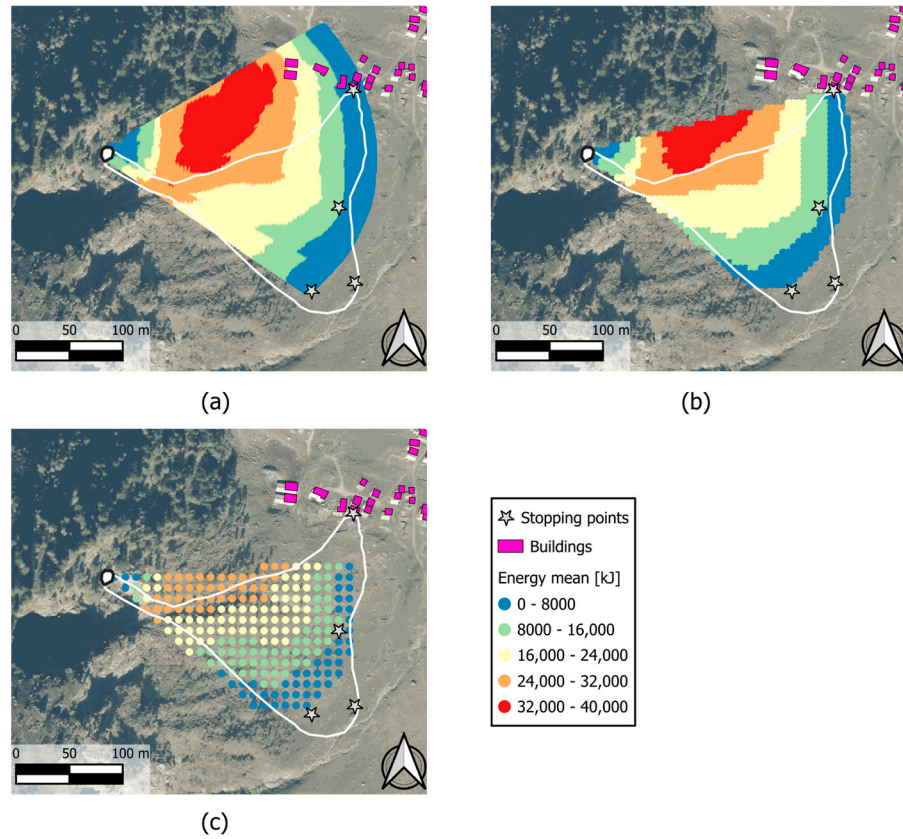


Figure 11. *Drocka_Basic* results of the back-analysis of the rockfall event, influence of DTM cell size: (a) cell size: 1 m; (b) cell size: 5 m; and (c) cell size: 10 m.

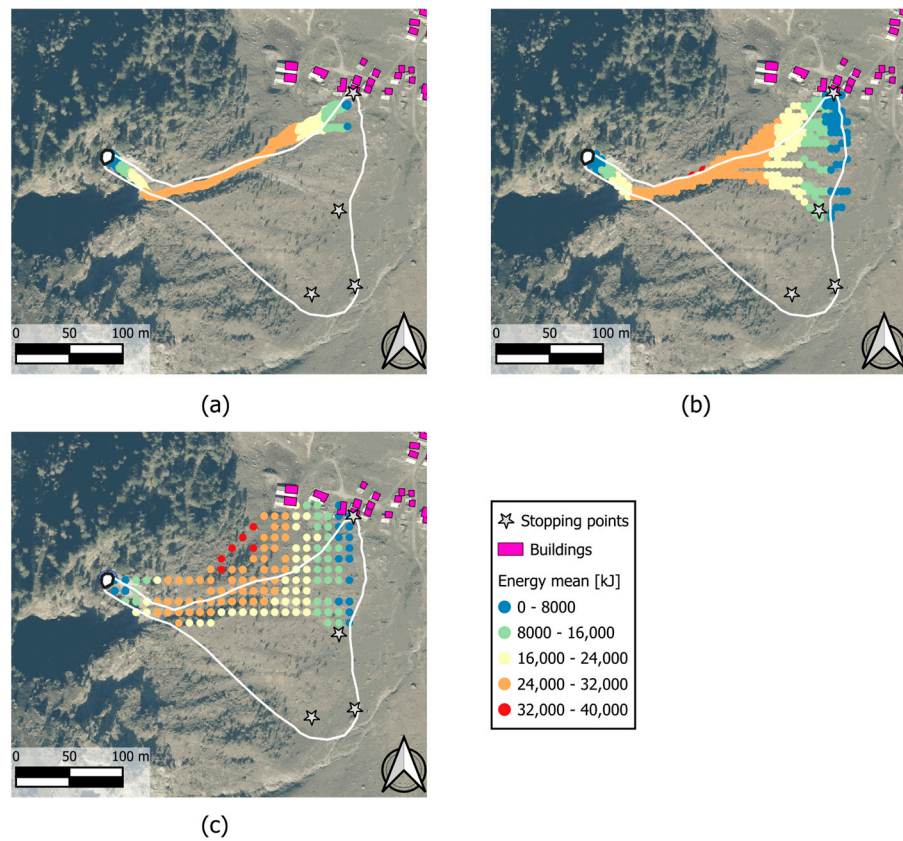


Figure 12. *Drocka_Flow* results of the back-analysis of the rockfall event, influence of DTM cell size: (a) cell size: 1 m; (b) cell size: 5 m; and (c) cell size: 10 m.

3.2. Susceptibility and Relative (Spatial) Hazard Analysis

To exemplify the suggested procedure for the susceptibility analysis, this study was extended to the slope surrounding the area where the buildings are located. Since no information was available to quickly identify the possible source areas, all DTM cells with an inclination greater than a specific threshold were selected on the slope above the buildings. Following [46], the resulting threshold is 49° for a 5 m DTM. A total of 80 source points was randomly selected within cells exceeding this threshold, covering a slope sector approximately 200 m in length, as shown in Figure 13a. Finally, a block with a volume of 1 m^3 was used to estimate the kinetic energy.

Figure 13b compares the results of the analyses conducted with *Rockfall–Droka* modules in terms of runout area, while Figure 13c,d show the mean kinetic energy obtained by the two modules. To assess the rockfall susceptibility, the *Droka_Basic* spatial frequency results, defined as the number of overlapping cones out of the total source points (Figure 14a), were multiplied by the mean kinetic energy values (Figure 13c) at each point. The final output, shown in Figure 14b, highlights the most critical zones by combining both the spatial frequency and phenomenon intensity and can be interpreted as a relative (spatial) hazard.

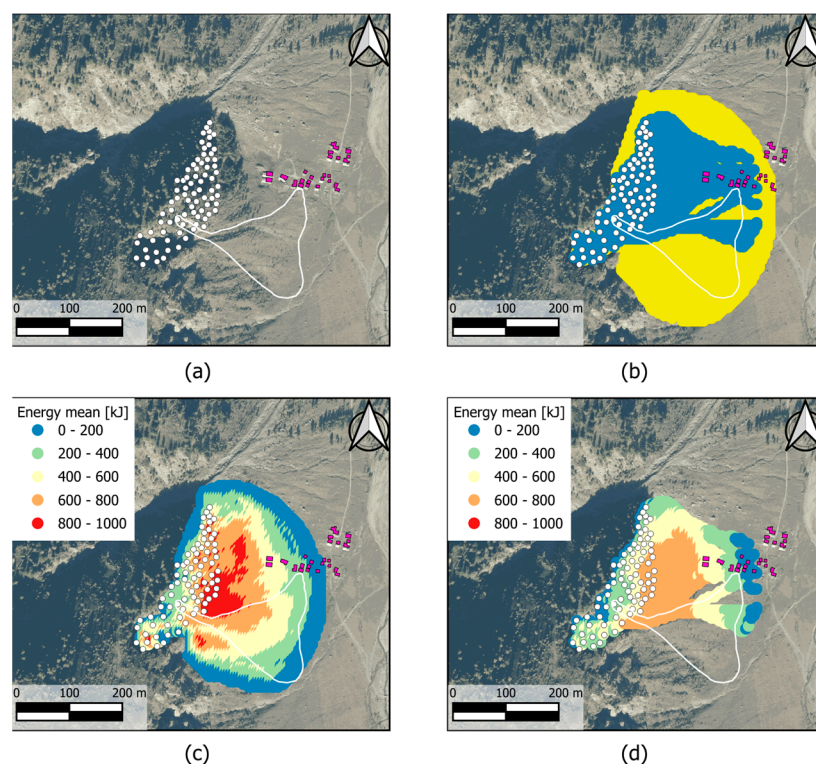


Figure 13. Susceptibility analysis for the Bobbio Pellice case study: (a) source points distribution in white and location of the buildings in magenta—the white envelope represents the invasion area of the 24 June 2024 rockfall event; (b) runout areas by *Droka_Basic* (yellow) and *Droka_Flow* (blue); (c) mean kinetic energy, *Droka_Basic*; and (d) mean kinetic energy, *Droka_Flow*.

The comparison between the results from *Droka_Basic* and *Droka_Flow* again confirms the consistency of the two algorithms. *Droka_Basic* is more conservative regarding total the invasion area (Figure 13b) and mean kinetic energy (Figure 13c,d), as the area covered by rockfall paths simulated by *Droka_Flow* (Figure 13b) is concentrated in the northern part of the invasion zone and shows lower mean kinetic energy values in the central region. However, *Droka_Basic* indicates the highest frequency in this central zone (Figure 14a), suggesting that blocks from multiple source points can reach it. Differences in the mean kinetic energy calculated by the two algorithms arise from statistical com-

parisons based on different sample populations, although the maximum kinetic energy values computed are identical across the entire area. Regarding the slope susceptibility and relative (spatial) hazard, the results from both algorithms are again consistent, highlighting the critical situation for certain buildings. This finding underscores the need for a more detailed analysis to accurately assess the risk to these structures and to establish appropriate mitigation measures.

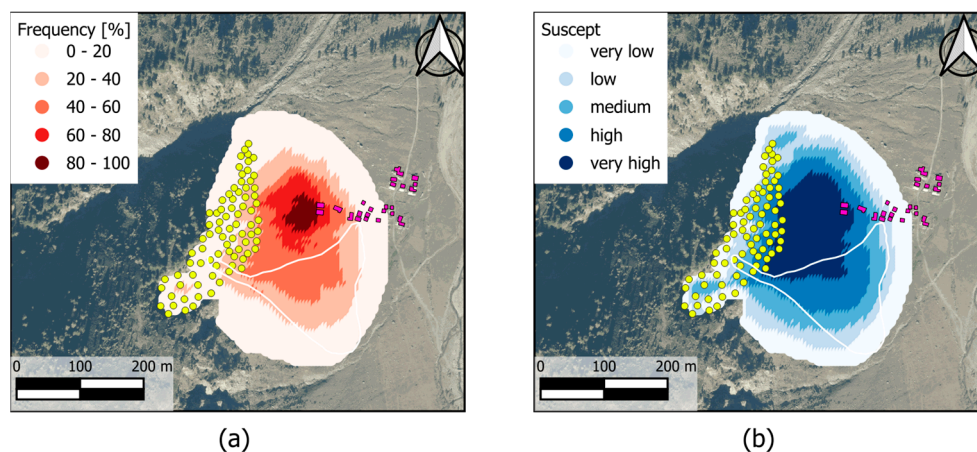


Figure 14. Susceptibility analysis for the Bobbio Pellice case study: (a) rockfall frequency; and (b) relative (spatial) hazard. Yellow dots represent source points.

4. Discussion

The assessment of the landslide susceptibility and hazard is crucial for territorial management and risk mitigation. At medium to small scales, such as roads, municipalities, or provincial areas, empirical or simplified analytical methods are commonly used to identify critical areas requiring detailed investigation [10]. Numerous methodologies exist for small-scale analyses using territorial data; most have been implemented within GIS environments due to their analytical capabilities and the growing availability of public spatial datasets.

However, there is still a lack of a comprehensive GIS plugin capable of analyzing various landslide types, including slope susceptibility, hazard assessment, affected areas, and associated energy. In this context, the *Geohazard* plugin was developed as an open-source, user-friendly tool for preliminary landslide susceptibility and hazard assessments at medium to small scales within the QGIS environment. The current version includes three modules tailored to different landslide hazard aspects, described in Section 2, with application examples provided to facilitate the discussion.

The *Groundmotion-C Index* (Section 2.1) module reliably classified slopes based on their visibility from satellite orbits, effectively managing uncertainties in SAR data interpretation for slow slope movements. Validation using a training dataset confirmed the accuracy of the module, highlighting its utility for the long-term monitoring of gravitational processes.

The *Landslide-Shalstab* module (Section 2.2) assessed shallow landslide susceptibility by calculating critical rainfall infiltration q_{cr} across large areas. The analysis produced susceptibility maps that aligned with prior hazard studies, illustrating its reliability. These maps provide a foundation for further analyses, such as evaluating the landslide runout and kinetic energy, which are essential for defining hazard scenarios. However, the application of the *Shalstab* model to DTMs with different resolutions has revealed its sensitivity to this parameter. High-resolution DTMs can capture fine-scale terrain features, enabling precise calculations of slope gradients and contributing areas. In contrast, lower-resolution DTMs may smooth out critical topographic details, potentially leading to less reliable predictions

and the potential overestimation or underestimation of hazard zones [47]. Accurate predictions also depend on the precision and accuracy in estimating hydrological and mechanical parameters and their spatial distribution, a key point when analyzing extensive areas. Therefore, for *Shalstab* applications, a balanced approach that combines an appropriate DTM resolution with accurate parameter estimations is crucial. This ensures the reliable identification of shallow landslide-prone areas and supports informed decision-making in land-use planning and hazard mitigation. The *Rockfall–Droka_Basic* and *Droka_Flow* modules (Section 2.3) proved effective in evaluating rockfall hazards. By calibrating parameters, the modules delineated invasion zones and estimated the kinetic energy, offering complementary perspectives. *Droka_Basic* provided an overall depiction of the hazard area, while *Droka_Flow* simulated specific trajectories, enhancing our understanding of the relative hazard dynamics. The influence of the DTM resolution was analyzed in the paper, emphasizing the importance of calibrating model parameters according to DTM cell resolutions. When detailed information about past events is available for the study area, as shown in the Bobbio Pellice case study, performing a back-analysis on the same DTM used for the predictive analysis of the entire region enhances the robustness of the calibration process.

The proposed *Geohazard* plugin offers an innovative approach to preliminary landslide susceptibility and hazard assessment by integrating multiple analytical modules within the QGIS environment. Unlike previous methodologies that typically address isolated aspects of landslide analysis, this plugin combines slope susceptibility, critical rainfall infiltration, and rockfall impact zones' evaluation in a unified platform. This integrated framework facilitates a more comprehensive hazard assessment while simplifying the workflow for geohazard studies.

5. Conclusions

The *Geohazard* plugin, presented in this paper, integrates multiple modules to address different aspects of geohazard analysis, offering a practical and versatile framework for hazard management at medium to small scales.

The *Groundmotion–C Index* module demonstrated its reliability during validation on a training dataset with a 25 m cell size DTM, where its results closely matched manual calculations. The application results further illustrated the ability to classify slopes based on their visibility from the satellite orbit, providing a valuable tool for reducing uncertainties in SAR data interpretation for the slow slope movement estimation.

The *Landslide–Shalstab* module effectively assessed the susceptibility to shallow landslides by calculating the critical rainfall infiltration required to trigger slope instability. Its application to the Deago area (located in the hilly Langhe region, northwestern Italy) demonstrated the results of the analysis at a small scale and the validation, based on hazard maps developed in previous studies [39]. The critical rainfall map q_{cr} and the resulting susceptibility classifications provided valuable insights into the spatial distribution of instability conditions. Further improvements to this method could include the implementation of a simplified infiltration model to express the results in terms of gross rainfall. This information is essential for defining potential landslide scenarios and forms the basis for subsequent analyses of the affected areas and process intensity, contributing to the overall calculation of the landslide hazard.

The *Rockfall–Droka_Basic* and *Droka_Flow* modules, designed for rockfall analysis, were tested in the Bobbio Pellice case study, an area in the Italian Western Alps [44]. Parameter calibration based on a well-documented rockfall event in the Bobbio Pellice area enabled the accurate delineation of invasion zones and the identification of critical trajectories. *Droka_Basic* captured the overall invasion zone using energy and lateral spreading angles,

while *Droka_Flow* simulated individual trajectories, both providing preliminary estimates of block velocities and kinetic energy. The results showed that the destroyed building in the area was in a critical zone, where the estimated block kinetic energy exceeded 5000 kJ. The case study showed how the modules perform under real case studies. The calibration process, grounded in field observations, emphasized the critical importance of systematically aligning model inputs with observed data to enhance their accuracy. Additionally, the results showed that the modules can replicate observed events, offering important insights into trajectory precision and hazard mapping. The findings also stressed the importance of maintaining consistency between the DTM used for calibration and the one applied in the analysis to ensure consistent and reliable results, supporting better hazard prediction and land-use planning. Future research will focus on addressing these sensitivities to further improve the applicability and robustness of the plugin. The two modules were complementary, with *Droka_Basic* delineating the overall invasion area and *Droka_Flow* providing detailed insights into critical trajectories.

These findings validate the *Geohazard* plugin as a reliable and versatile tool for geohazard assessment. By integrating multiple analytical approaches, the plugin enhances our understanding of slope instability and aids in developing effective risk mitigation strategies. Looking ahead, the *Geohazard* plugin will be expanded to include additional modules specifically tailored for territorial landslide analysis, with a particular focus on diffuse and recurrent phenomena. Planned improvements include tools for slope classification related to rockfall susceptibility, defined as the propensity of a slope to trigger rockfall events. Additionally, the integration of triggering and run-out modules will provide a comprehensive analytical framework suitable for various types of landslides. A simplified tool for assessing the vulnerability of different types of exposed elements will also be introduced, enabling a preliminary estimation of landslide risk at medium to small scales.

Finally, the possibility of the integration of machine-learning modules for landslide susceptibility mapping [48] will be explored to enhance predictive accuracy and facilitate the incorporation of diverse environmental and geospatial datasets into the analysis.

In a time of increasing hydrogeological instability driven by climate change, the need for effective prevention strategies has become a critical priority for protecting both people and infrastructure from hazardous events. Prevention, as a key aspect of climate change adaptation, requires proactive measures to reduce the impacts of geohazards. This work aims to support and enhance prevention strategies, which are essential in the context of vulnerable territories such as Italy, where almost 94% of the Italian municipalities are at risk of landslides, floods, and coastal erosion, with over 8 million people living in high-hazard areas [49].

Author Contributions: Conceptualization, M.C., A.F. and S.C.; methodology, M.C., A.F., G.T., S.C. and R.P.; software, A.F. and C.F.; validation, M.C., A.F., C.F. and S.C.; resources, M.C. and R.P.; data curation, A.F., S.C. and R.P.; writing—original draft preparation, M.C., A.F., S.C. and G.T.; writing—review and editing, G.T.; supervision, M.C. and R.P. All authors have read and agreed to the published version of the manuscript.

Funding: This research received no external funding.

Data Availability Statement: The plugin is available at <https://github.com/Arpapiemonte/geohazard> (accessed on 15 January 2025) and in the official QGIS plugin repository. Datasets used for the validation of the models are available at the same link.

Conflicts of Interest: The authors declare no conflicts of interest.

References

1. Seneviratne, S.I.N.; Nicholls, D.; Easterling, C.M.; Goodess, S.; Kanae, J.; Kossin, Y.; Luo, J.; Marengo, K.; McInnes, M.; Rahimi, M.; et al. Changes in climate extremes and their impacts on the natural physical environment. In *Managing the Risks of Extreme Events and Disasters to Advance Climate Change Adaptation*; Field, C.B., Barros, V., Stocker, T.F., Dahe, Q., Dokken, D.J., Ebi, K.L., Mastrandrea, M.D., Mach, K.J., Plattner, G.-K., Allen, S.K., et al., Eds.; A Special Report of Working Groups I and II of the Intergovernmental Panel on Climate Change (IPCC); Cambridge University Press: Cambridge, UK; New York, NY, USA, 2012; pp. 109–230.
2. Crozier, M.J. Deciphering the effect of climate change on landslide activity: A review. *Geomorphology* **2010**, *124*, 260–267. [[CrossRef](#)]
3. Picarelli, L.; Lacasse, S.; Ho, K.K. The impact of climate change on landslide hazard and risk. In *Understanding and Reducing Landslide Disaster Risk: Volume 1 Sendai Landslide Partnerships and Kyoto Landslide Commitment*; Springer: Berlin/Heidelberg, Germany, 2021; pp. 131–141.
4. Fell, R.; Corominas, J.; Bonnard, C.; Cascini, L.; Leroi, E.; Savage, W.Z. Guidelines for landslide susceptibility, hazard and risk zoning for land-use planning. *Eng. Geol.* **2008**, *102*, 99–111. [[CrossRef](#)]
5. Van Westen, C.J.; Castellanos, E.; Kuriakose, S.L. Spatial data for landslide susceptibility, hazard, and vulnerability assessment: An overview. *Eng. Geol.* **2008**, *102*, 112–131. [[CrossRef](#)]
6. Ferlisi, S.; Gullà, G.; Nicodemo, G.; Peduto, D. A multi-scale methodological approach for slow-moving landslide risk mitigation in urban areas, southern Italy. *EuroMediterr. J. Environ. Integr.* **2019**, *4*, 1–15. [[CrossRef](#)]
7. Varnes, D.J. Landslide types and processes. *Landslides Eng. Pract.* **1958**, *24*, 20–47.
8. Hungr, O. Dynamics of rapid landslides. In *Progress in Landslide Science*; Sassa, K., Fukuoka, H., Wang, F., Wang, G., Eds.; Springer: Berlin/Heidelberg, Germany, 2007. [[CrossRef](#)]
9. Lacasse, S.; Nadim, F.; Lacasse, S.; Nadim, F. Landslide risk assessment and mitigation strategy. In *Landslides—Disaster Risk Reduction*; Springer: Berlin/Heidelberg, Germany, 2009; pp. 31–61. [[CrossRef](#)]
10. Scavia, C.; Barbero, M.; Castelli, M.; Marchelli, M.; Peila, D.; Torsello, G.; Vallero, G. Evaluating rockfall risk: Some critical aspects. *Geosciences* **2020**, *10*, 98. [[CrossRef](#)]
11. Van Westen, C.J. Remote sensing and GIS for natural hazards assessment and disaster risk management. *Treatise Geomorphol.* **2013**, *3*, 259–298.
12. Filipello, A.; Giuliani, A.; Mandrone, G. Rock Slopes Failure Susceptibility Analysis: From Remote Sensing Measurements to Geographic Information System Raster Modules. *Am. J. Environ. Sci.* **2010**, *6*, 489–494.
13. Poursanidis, D.; Chrysoulakis, N. Remote Sensing, natural hazards and the contribution of ESA Sentinels missions. *Remote Sens. Appl. Soc. Environ.* **2017**, *6*, 25–38. [[CrossRef](#)]
14. Noviello, C.; Verde, S.; Zamparelli, V.; Fornaro, G.; Pauciuillo, A.; Reale, D.; Nicodemo, G.; Ferlisi, S.; Gullà, G.; Peduto, D. Monitoring buildings at landslide risk with SAR: A methodology based on the use of multipass interferometric data. *IEEE Geosci. Remote Sens. Mag.* **2020**, *8*, 91–119. [[CrossRef](#)]
15. Guzzetti, F.; Carrara, A.; Cardinali, M.; Reichenbach, P. Landslide hazard evaluation: A review of different approaches. *Earth Sci. Rev.* **2005**, *79*, 147–181.
16. Cruden, D.M.; Varnes, D.J. Landslide Types and Processes, Transportation Research Board, U.S. National Academy of Sciences, Special Report. *Spec. Rep. Natl. Res. Counc. Transp. Res. Board* **1996**, *247*, 36–75.
17. Evans, S.G.; Hungr, O.; Clague, J.J. Dynamics of the 1984 rock avalanche and associated distal debris flow on Mount Cayley, British Columbia, Canada; implications for landslide hazard assessment on dissected volcanoes. *Eng. Geol.* **2001**, *61*, 29–51. [[CrossRef](#)]
18. Meissl, G. Modelling the runout distances of rockfall using a geographic information system. *Z. Geomorphol. Suppl.* **2001**, *125*, 129–137.
19. Wichmann, V. The Gravitational Process Path (GPP) model (v1. 0)—A GIS-based simulation framework for gravitational processes. *Geosci. Model Dev.* **2017**, *10*, 3309–3327. [[CrossRef](#)]
20. Carrara, A.; Cardinali, M.; Detti, R.; Guzzetti, F.; Pasqui, V.; Reichenbach, P. Geographical Information Systems and Multivariate Model in Landslide Hazard Evaluation. *Alps* **1990**, *90*, 17–28.
21. Castelli, M.; Tosello, G.; Vallero, G. Preliminary Modeling of Rockfall Runout: Definition of the Input Parameters for the QGIS Plugin QPROTO. *Geosciences* **2021**, *11*, 88. [[CrossRef](#)]
22. Pack, R.T.; Tarboton, D.G.; Goodwin, C.N. The SINMAP Approach to Terrain Stability Mapping. In *8th Congress of the International Association of Engineering Geology, Vancouver, BC, Canada, 21–25 September 1998*; Moore, D., Hungr, O., Eds.; Vol. 2: Engineering Geology and Natural Hazards; A A Balkema: Amsterdam, The Netherlands, 1998; pp. 1157–1166, ISBN-10: 9054109920.
23. Montgomery, D.R.; Dietrich, W.E. A physically-based model for the topographic control of shallow landsliding. *Water Resour. Res.* **1994**, *30*, 1153–1171. [[CrossRef](#)]
24. Ji, J.; Cui, H.; Zhang, T.; Song, J.; Gao, Y. A GIS-based tool for probabilistic physical modelling and prediction of landslides: GIS-FORM landslide susceptibility analysis in seismic areas. *Landslides* **2022**, *19*, 2213–2223. [[CrossRef](#)]

25. Alvioli, M.; Baum, R.L. Parallelization of the TRIGRS model for rainfall-induced landslides using the message passing interface. *Environ. Model. Softw.* **2016**, *81*, 122–135. [CrossRef]
26. *R.slope.stability*. Available online: <https://www.landslidemodels.org/r.slope.stability/manual.php> (accessed on 15 January 2025).
27. *R.slopeunits*. Available online: <https://geomorphology.irpi.cnr.it/tools/slope-units> (accessed on 15 January 2025).
28. *Geohazard* Plugin. Available online: <https://github.com/Arpapiemonte/geohazard> (accessed on 15 January 2025).
29. Notti, D.; Herrera, G.; Bianchini, S.; Meisina, C.; García-Davalillo, J.C.; Zucca, F. A methodology for improving landslide PSI data analysis. *Int. J. Remote Sens.* **2014**, *35*, 2186–2214. [CrossRef]
30. Jaboyedoff, M.; Labiouse, V. Preliminary estimation of rockfall runout zones. *Nat. Hazards Earth Syst. Sci.* **2011**, *11*, 819–828. [CrossRef]
31. Copernicus—European Ground Motion Service. Available online: <https://egms.land.copernicus.eu/> (accessed on 15 January 2025).
32. Montini, G. *Linee Guida per L'utilizzo dei Dati di Deformazione (PS) Derivati da Analisi Multi-Interferometrica di Immagini Radar Satellitari*; Technical Report; Geoprofessionis sas: Francavilla al Mare, Italy, 2019; pp. 2–5, 8–9, 15–19, 30–34. (In Italian)
33. Ren, T.; Gong, W.; Bowa, V.M.; Tang, H.; Chen, J.; Zhao, F. An improved R-Index model for terrain visibility analysis for landslide monitoring with InSAR. *Remote Sens.* **2021**, *13*, 1938. [CrossRef]
34. Cignetti, M. State of activity classification of deep-seated gravitational slope deformation at regional scale based on Sentinel-1 data. *Landslide* **2023**, *20*, 7–9. [CrossRef]
35. Colesanti, C.; Wasoski, J. Investigating landslides with space-borne Synthetic Aperture Radar (SAR) interferometry. *Eng. Geol.* **2006**, *88*, 173–199. [CrossRef]
36. Plank, S.; Singer, J.; Minet, C.; Thuro, K. Pre-survey suitability evaluation of the differential synthetic aperture radar interferometry method for landslide monitoring. *Int. J. Remote Sens.* **2012**, *33*, 6623–6637. [CrossRef]
37. Regione Piemonte Geoportale. Available online: <https://geoportale.igr.piemonte.it/cms/> (accessed on 15 January 2025).
38. Dietrich, W.E.; Montgomery, D.R. SHALSTAB: A Digital Terrain Model for Mapping Shallow Landslide Potential. Technical Report NCAS. 1998. Available online: <https://calm.geo.berkeley.edu/geomorph/shalstab/index.htm> (accessed on 15 January 2025).
39. Campus, C.; Forlati, F.; Nicolò, G. Note illustrative della Carta della pericolosità per instabilità dei versanti. Foglio 211 (DEGO). APAT, Agenzia Regionale per la Protezione dell'Ambiente e per i Servizi Tecnici. Litografia Geda, Nichelino (TO). *Foglio* **2005**, *211*, 234. (In Italian)
40. Interreg, B., III. CatchRisk-Mitigation of Hydro-geological Risk in Alpine Catchments. 2005. Available online: <https://www.arpa.piemonte.it/sites/default/files/media/2023-10/catch2005.pdf> (accessed on 15 January 2025).
41. Green, W.H.; Ampt, G. Studies of soil physics, part I—The flow of air and water through soils. *J. Agric. Sci.* **1911**, *4*, 1–24.
42. Campus, S.; Forlati, F.; Nicolò, G.; Fontan, D.; Gelati, R.; Joannas, J.; Morelli, M.; Piana, F.; Rabuffetti, D. Note illustrative della carta della pericolosità per instabilità dei versanti alla scala 1:50.000, foglio 211 DEGO. Available online: https://www.isprambiente.gov.it/Media/carg/note_illustrative/211_Dego.pdf (accessed on 15 January 2025). (In Italian)
43. *R.drain*. Available online: <https://grass.osgeo.org/grass-stable/manuals/r.drain.html> (accessed on 15 January 2025).
44. GeoAlpi Consulting. Site Survey Report, 28 June 2024. 2024. Available online: <https://geopalpiconsulting.it/> (accessed on 15 January 2025). (In Italian)
45. Geoportale of the Italian Ministry of the Environment. Available online: <https://gn.mase.gov.it/portale/en/data-distribution-services-pst> (accessed on 15 January 2025).
46. Interreg 3a Alpi Latine. *Progetto 165 PROVIALP, Protezione della Viabilità Alpina—Final Report*; ARPA Piemonte: Turin, Italy, 2008. Available online: <https://www.arpa.piemonte.it/pubblicazione/progetto-n165-provialp-protezione-della-viabilita-alpina> (accessed on 15 January 2025). (In Italian and French)
47. Sbroglia, R.; Reginatto, G.; Higashi, R.; Guimarães, R. Mapping susceptible landslide areas using geotechnical homogeneous zones with different DEM resolutions in Ribeirão Baú basin, Ilhota/SC/Brazil. *Landslides* **2018**, *15*, 2093–2106. [CrossRef]
48. Yuke, H.; Song, L.; Khan, U.; Zhang, B. Stacking ensemble of machine learning methods for landslide susceptibility mapping in Zhangjiajie City, Hunan Province, China. *Environ. Earth Sci.* **2023**, *82*, 35.
49. Trigila, A.; Iadanza, C.; Lastoria, B.; Bussetini, M.; Barbano, A. *Dissesto Idrogeologico in Italia: Pericolosità e Indicatori di Rischio—Edizione 2021*; ISPRA Rapporti: Roma, Italy, 2021. (In Italian)

Disclaimer/Publisher's Note: The statements, opinions and data contained in all publications are solely those of the individual author(s) and contributor(s) and not of MDPI and/or the editor(s). MDPI and/or the editor(s) disclaim responsibility for any injury to people or property resulting from any ideas, methods, instructions or products referred to in the content.